



GEOCHEMISTRY

Mercury isotopes show vascular plants had colonized land extensively by the early Silurian

Wei Yuan^{1†}, Mu Liu^{2†}, Daizhao Chen^{2,3*}, Yao-Wu Xing⁴, Robert A. Spicer^{4,5,6}, Jitao Chen^{7,8}, Theodore R. Them II⁹, Xun Wang¹, Shizhen Li¹⁰, Chuan Guo¹¹, Gongjing Zhang¹², Liyu Zhang¹³, Hui Zhang¹, Xinbin Feng^{1,3*}

The colonization and expansion of plants on land is considered one of the most profound ecological revolutions, yet the precise timing remains controversial. Because land vegetation can enhance weathering intensity and affect terrigenous input to the ocean, changes in terrestrial plant biomass with distinct negative $\Delta^{199}\text{Hg}$ and $\Delta^{200}\text{Hg}$ signatures may overwrite the positive Hg isotope signatures commonly found in marine sediments. By investigating secular Hg isotopic variations in the Paleozoic marine sediments from South China and peripheral paleocontinents, we highlight distinct negative excursions in both $\Delta^{199}\text{Hg}$ and $\Delta^{200}\text{Hg}$ at Stage level starting in the early Silurian and again in the Carboniferous. These geochemical signatures were driven by increased terrestrial contribution of Hg due to the rapid expansion of vascular plants. These excursions broadly coincide with rising atmospheric oxygen concentrations and global cooling. Therefore, vascular plants were widely distributed on land during the Ordovician-Silurian transition (~444 million years), long before the earliest reported vascular plant fossil, *Cooksonia* (~430 million years).

INTRODUCTION

The colonization of land by plants during the Paleozoic had far-reaching impacts on global biogeochemical cycles by enhancing silicate weathering and carbon burial, subsequently affecting atmospheric $p\text{O}_2$ and $p\text{CO}_2$ levels (1). The establishment of land ecosystems was also closely related to the major pedogenesis and sediment stability, which, in turn, influenced river systems and landscapes on Earth's surface (2). This evolutionary leap of complex life from water to land greatly affected terrestrial landscapes and the evolutionary trajectory of Earth's surface environments.

Fossil evidence suggests that the greening of the landscape by early autotrophs can be broadly divided into four overlapping phases (3). The first phase probably began in the late

Mesoproterozoic to early Neoproterozoic and mainly involved microbial mats on bare mineral surfaces and in lake systems. The second phase was characterized by bryophyte-grade revolution in the Ordovician. The third phase, the onset of which is investigated here, marks the occurrence and potential expansion of early vascular plants during the Ordovician-Silurian transition. The fourth phase represents the first major diversification of land plant architecture and life habits possibly as early as in the Silurian Ludlow Epoch. On the other hand, molecular clock calculations suggest that the highest probability of embryophyte origin is within the Cambrian (4) despite debates of the evolutionary relationships between the living bryophytes and tracheophytes (5). Nevertheless, there is still no consensus on the precise time scale for critical steps in the land colonization of complex life due to relative lack of terrestrial sediments of facies suited to fossil preservation (6).

Although early land plant fossils are fragile, often fragmentary, rare, extremely small, and difficult to identify as plant material, indirect fingerprints of land plants in the form of inorganic and organic geochemical markers (7) have the potential to be identified in sediments. The biogeochemical cycling of mercury (Hg) archived in sedimentary rocks has offered an effective approach for identifying distinct events in geological history, such as intensified volcanic episodes (8), enhanced terrestrial input in marine environments (9), or photic zone euxinia (10). Apart from Hg concentrations, Hg stable isotope compositions can be used for distinguishing various sources or processes controlling Hg accumulation in depositional systems (8, 11).

Mercury isotope systematics comprise both mass-dependent fractionation (MDF; reported as $\delta^{202}\text{Hg}$) and mass-independent fractionation (MIF; reported as $\Delta^{199}\text{Hg}$ and $\Delta^{201}\text{Hg}$ for odd-MIF, and $\Delta^{200}\text{Hg}$ for even-MIF). The Hg odd-MIF transitions can be triggered by active Hg^{II} photochemical (reduction) processes in aqueous solutions, methylmercury (MeHg) photodegradation, abiotic dark redox reactions, and photo-oxidation processes [e.g., (11)]. In contrast, even-MIF ($\Delta^{200}\text{Hg}$) is almost exclusively related

¹State Key Laboratory of Environmental Geochemistry, Institute of Geochemistry, Chinese Academy of Sciences, Guiyang 550081, China. ²Key Laboratory of Cenozoic Geology and Environment, Institute of Geology and Geophysics, Chinese Academy of Sciences, Beijing 100029, China. ³University of Chinese Academy of Sciences, Beijing 100049, China. ⁴CAS Key Laboratory of Tropical Forest Ecology, Xishuangbanna Tropical Botanical Garden, Chinese Academy of Sciences, Mengla, Yunnan 666303, China. ⁵School of Environment, Earth and Ecosystem Sciences, The Open University, Milton Keynes, MK7 6AA, UK. ⁶State Key Laboratory of Tibetan Plateau Earth System, Resources and Environment (TPESRE), Institute of Tibetan Plateau Research, Chinese Academy of Sciences, Beijing 100101, China. ⁷State Key Laboratory of Palaeobiology and Stratigraphy, Nanjing Institute of Geology and Palaeontology and Center for Excellence in Life and Palaeoenvironment, Chinese Academy of Sciences, Nanjing 210008, China. ⁸Nanjing College, University of Chinese Academy of Sciences, Nanjing 211135, China. ⁹Department of Geology and Environmental Geosciences, College of Charleston, Charleston, SC 29424, USA. ¹⁰Oil and Gas Survey, China Geological Survey, Ministry of Natural Resources, Beijing 100083, China. ¹¹College of Resources and Environmental Engineering, Key Laboratory of Karst Georesources and Environment, Ministry of Education, Guizhou University, Guiyang 550025, China. ¹²Department of Earth Science and Engineering, Tsinghua University of Technology, Beijing 100084, China. ¹³Wuxi Research Institute of Petroleum Geology, Petroleum Exploration and Production Research Institute, SINOPEC, Wuxi 214126, China.

*Corresponding author. Email: fengxinbin@vip.skleg.cn (X.F.); dzh-chen@mail.jiggcas.ac.cn (D.C.)

†These authors contributed equally to this work.

to upper tropospheric and/or stratospheric photochemical reactions (11, 12). Hg^{II} with positive odd- and even-MIF accumulations in rainfall can induce higher MIF values, which can be preserved in ancient marine sediments. In addition, the aqueous photoreduction could also lead to the positive residual Hg^{II} deposited in seafloor. The primarily negative MIF signatures, which dominantly occur in the atmospheric Hg^0 reservoir, can be sequestered by vegetation in terrestrial ecosystems and then transported into marine sediments (Fig. 1). For this research on sedimentary rock, it has been demonstrated that negligible MIF transformations occur under high-temperature and high-pressure conditions (13, 14), indicating that original MIF signals are resistant to subsequent diagenetic or thermal maturation effects.

Unlike the relatively stable contribution of atmospheric Hg^{II} to land, the amount of Hg cycled by plant and volcanic sources can be highly variable. In the modern Hg cycle, nearly 3000 Mg Hg is sequestered into the terrestrial ecosystem annually from the atmosphere via plants, representing ~60% of the total atmospheric reservoir of ~5000 Mg (15). Moreover, the global terrestrial Hg input flux of $0.09 \text{ Mg year}^{-1}$ is $1.5\times$ higher and $0.5\times$ lower than the flux of Hg into ocean sediments, with $0.06 \text{ Mg year}^{-1}$ for coastal sediment and $0.18 \text{ Mg year}^{-1}$ for pelagic sediments, respectively (16). Comparatively, for those intervals in Phanerozoic history not associated with extreme events such as large igneous province (LIP) volcanism, terrestrial input was likely the governing variable that controlled the Hg isotopic signature of proximal marine sediments.

To establish the temporal framework for the evolution and expansion of early land plants and explore their relationship with secular changes in atmospheric chemistry, we investigated the Hg concentration and isotopic signatures of marine sedimentary rock samples collected from modern day South China and peripheral paleocontinents spanning from the Cambrian to Permian (fig. S1). The contribution of plant composition in each period was further quantified using a two end-member, stable isotope mixing model. A process of land vegetation expansion beginning in the early Silurian

is highlighted as driving substantial increases of land-derived Hg into the marine sedimentary system.

RESULTS

Hg mixing model and uncertainties

An isotope-mixing model with two end members was applied to the dataset, aiming to budget the variation in the relative contribution of land plants during the Paleozoic. The Hg in marine sediments is dominantly derived from three main sources: (i) atmospheric Hg^{II} input through precipitation and particulate matter deposition; (ii) terrigenous input, which is composed of immobilized atmospheric Hg^0 by foliage, including wildfire, deforestation, and so on; and (iii) "geological" Hg, including bedrock weathering and/or volcanic sources. Since the biogeochemical signature of the atmospheric Hg remains stable, terrigenous input is the governing variable that determines marine sediment Hg isotopic compositions, except during extreme events such as LIP emplacement. Therefore, this two end-member mixing model is expected to quantify the contribution from plant biomass and is calculated as follows

$$F_{\text{plant}} + F_{\text{non-plant}} = 1 \quad (1)$$

$$F_{\text{plant}} \times \Delta^{xxx}\text{Hg}_{\text{plant}} + F_{\text{non-plant}} \times \Delta^{xxx}\text{Hg}_{\text{non-plant}} = \Delta^{xxx}\text{Hg}_{\text{rock}} \quad (2)$$

where xxx represents Hg isotopes with mass number 199 or 201. F_{plant} and $F_{\text{non-plant}}$ represent the fraction of plant composition and non-plant composition, respectively. $\Delta^{xxx}\text{Hg}_{\text{plant}}$ represents the mean odd-MIF signatures of global foliage and litterfall ($\Delta^{199}\text{Hg} = -0.29 \pm 0.14\text{‰}$ and $\Delta^{201}\text{Hg} = -0.28 \pm 0.13\text{‰}$) (17), and $\Delta^{xxx}\text{Hg}_{\text{non-plant}}$ represents the most positive odd-MIF background signatures with $\Delta^{199}\text{Hg} = 0.20 \pm 0.10\text{‰}$ and $\Delta^{201}\text{Hg} = 0.18 \pm 0.12\text{‰}$ in samples from the Cambrian to Early Ordovician.

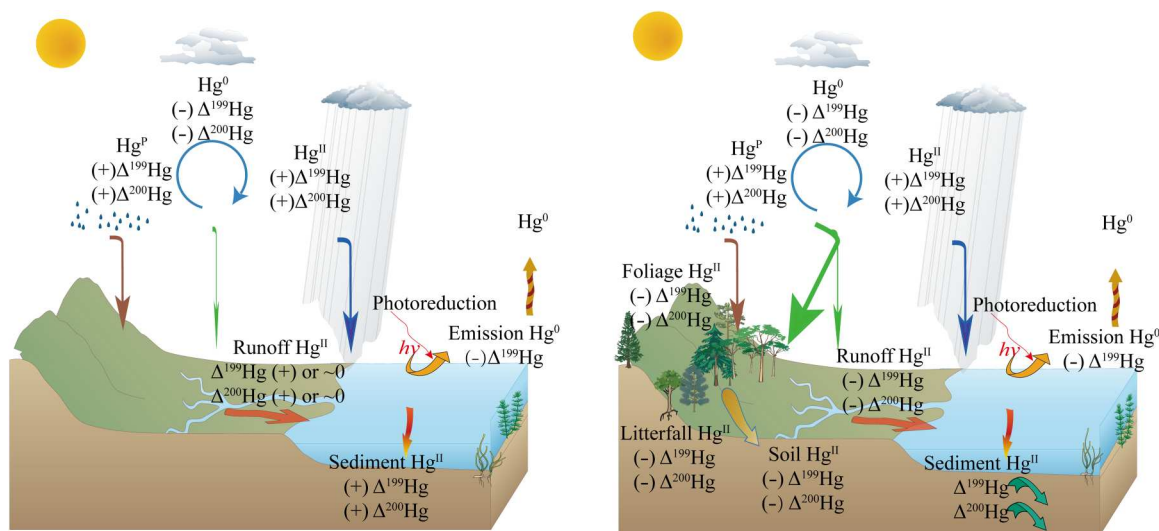


Fig. 1. Conceptual model showing Hg cycling on Earth. Model on left shows the Hg cycle without vascular plants on land, while the right shows the Hg cycle with vascular plants on land. Atmospheric Hg^0 can be sequestered by vascular plants in terrestrial ecosystems and then transported into marine sediments, leading to negative excursions in marine sediments.

Uncertainties in the model estimates come primarily from a lack of comprehensive understanding of the complete processes that contribute to the MIF shifts. First, the odd-MIF signatures of land plant contributions in the model were based on the measurement of modern plant samples. The dearth of Hg isotopic data from ancient foliage potentially limits model parameterization. Second, the odd-MIF signatures of marine sediments are characterized as positive, regardless of the negative odd-MIF signatures in sediments driven by sulfide photoreduction (10, 18). Third, possible long-term tectonic effects including the closing of the Paleo-Tethys were not considered in this model. Thus, the model outputs cannot be expected to represent precise quantifications of the global land vegetation areal coverage/biomass but refer to the relative contribution from land plants in coastal and riparian areas in the South China area and peripheral paleocontinents. The global distribution of land plants could be heterogeneous due to local geographic differences associated with the complexities of paleo-climate and environment. Last, some cited Hg isotopic data lack comprehensive petrographic characterization, leading to potential uncertainties in model estimation. We recommend that future geochemical studies should integrate more comprehensive geological descriptions.

A Paleozoic secular Hg isotope curve

In this study, dozens of replicate samples were derived from some typical profiles in each period, which can reduce the uncertainties caused by sampling and Hg isotope measurement. We mainly focus on broad isotopic trends and clustering observed at stage level. The slope of $\Delta^{199}\text{Hg}/\Delta^{201}\text{Hg}$ is nearly 1 (0.95 , $R^2 = 0.79$), suggesting the samples are potentially related to photo-induced redox reactions driven by magnetic isotope effects (Fig. 2 and fig. S2). The LOESS (locally estimated scatterplot smoothing) curves of both compiled odd-MIF ($\Delta^{199}\text{Hg}$) and even-MIF ($\Delta^{200}\text{Hg}$) datasets show a remarkable and continuous decreasing trend of $\Delta^{199}\text{Hg}$ and $\Delta^{200}\text{Hg}$ from the early Silurian to Carboniferous with minor oscillations (Fig. 3, A and B). These decreases indicate substantially elevated contributions of terrestrially derived Hg. In contrast, most of pre-Silurian samples yield consistently positive odd-MIF values with an average $\Delta^{199}\text{Hg}$ value of 0.11 and median value of 0.11, as well as an average $\Delta^{201}\text{Hg}$ value of 0.08 with a median value of 0.07.

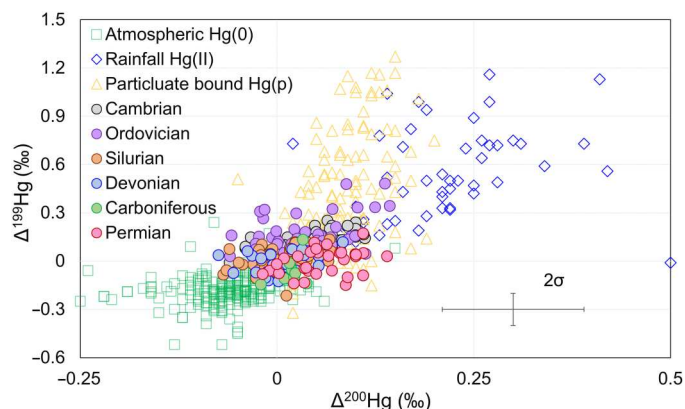


Fig. 2. Odd-MIF ($\Delta^{199}\text{Hg}$) versus even-MIF ($\Delta^{200}\text{Hg}$) compilation dataset from Paleozoic marine sediments and essential sources of Hg in modern environments. The values of sediments are available in data file S1. Values of atmospheric Hg^0 , rainfall Hg^{II} , and particulate bound Hg^{p} are from the (12).

Most of post-Silurian samples show near-zero MIF signatures, in which $\Delta^{199}\text{Hg}$ values average -0.01 with a median of 0.02 and $\Delta^{201}\text{Hg}$ values average -0.01 with a median of -0.08 . The $\Delta^{200}\text{Hg}$ dataset, most of which was derived from post-Silurian samples, clusters close to zero, although slight fluctuations occur in the Carboniferous and Early Permian.

Although our individual Hg isotopic datasets may encompass the effects of a number of environmental factors, the observation that negative MIF values have been solely reported in materials related to the terrestrial cycling of Hg except for photic zone euxinia, the long-term decreasing trend of $\Delta^{199}\text{Hg}$ during the Paleozoic Era toward negative values can be attributed to changes in the relative contribution and the isotopic signatures of terrigenous material. Moreover, the concomitant decreasing $\Delta^{200}\text{Hg}$ trend initiated in the Silurian also rules out the possibility that the $\Delta^{199}\text{Hg}$ decrease was related to changes in atmospheric cycling. In this light, a secular Hg isotope curve for the Paleozoic can be regarded as a reflection of the relative amount of contemporaneous terrestrial vascular plant biomass (Fig. 3, A and B).

A record of land plant expansion

The Paleozoic Era marks the establishment and radiation of land plants and thus the development of notable terrestrial biomass. The main types of colonization vary greatly over time. Excluding the potential isotopic effects from volcanism, weathering, and redox, positive Hg odd- and even-MIF values in the pre-Silurian samples retain signatures derived from rainfall Hg^{II} deposition, as the direct deposition of atmospheric Hg^0 was limited. The attenuation of global continental weathering intensity during the Paleozoic is suggested by decreasing $^{87}\text{Sr}/^{86}\text{Sr}$ values and the decoupled relationship between the Sr and Hg secular isotopic curves, also taking into account that the residence time differs between the two elements by millions of years (Fig. 4A). Thus, we suggest that secular variation in global terrestrial input intensity induced by large-scale tectonic events such as the closing of Paleo-Tethys was not the determining factor affecting Hg isotopes in the Paleozoic marine sediments of South China. In contrast to the Sr isotope curve, which is capable of tracking global tectonism, the Hg isotope curve should be considered a predominantly local signature controlled by sedimentary source-sink dynamics. The dominant source of Hg in terrestrial ecosystems is associated with the assimilation of atmospheric Hg^0 in vegetation, which is subsequently transferred to soils and watersheds after litterfall decomposition, and eventually influences the downstream marine ecosystem (12). Therefore, it is important to distinguish the effects of different terrestrial plant ecosystems at different times using the Hg isotopic values of sediments. Particularly, the coastal and riparian zones at lower latitudes, such as in South China, offered the preferential habitability of the hinterland for early vascular plants.

From the Early Cambrian to Middle Ordovician, MIF isotopic signatures are distinctly positive. In the Early Cambrian, $\Delta^{199}\text{Hg} = 0.13 \pm 0.06\text{‰}$ and $\Delta^{200}\text{Hg} = 0.04 \pm 0.04\text{‰}$ ($n = 41$); in the Middle Cambrian, $\Delta^{199}\text{Hg} = 0.13 \pm 0.04\text{‰}$ and $\Delta^{200}\text{Hg} = 0.05 \pm 0.02\text{‰}$ ($n = 6$); in the Late Cambrian, $\Delta^{199}\text{Hg} = 0.15 \pm 0.02\text{‰}$ and $\Delta^{200}\text{Hg} = 0.06 \pm 0.06\text{‰}$ ($n = 6$). These results show the comparable values with that in Edicaran period with $\Delta^{199}\text{Hg} = 0.15 \pm 0.06\text{‰}$ and $\Delta^{200}\text{Hg} = 0.02 \pm 0.03\text{‰}$ ($n = 106$). In the Early Ordovician, $\Delta^{199}\text{Hg} = 0.20 \pm 0.10\text{‰}$ and $\Delta^{200}\text{Hg} = 0.03 \pm 0.05\text{‰}$ ($n = 15$); and in the Middle Ordovician, $\Delta^{199}\text{Hg} = 0.20 \pm 0.13\text{‰}$ and

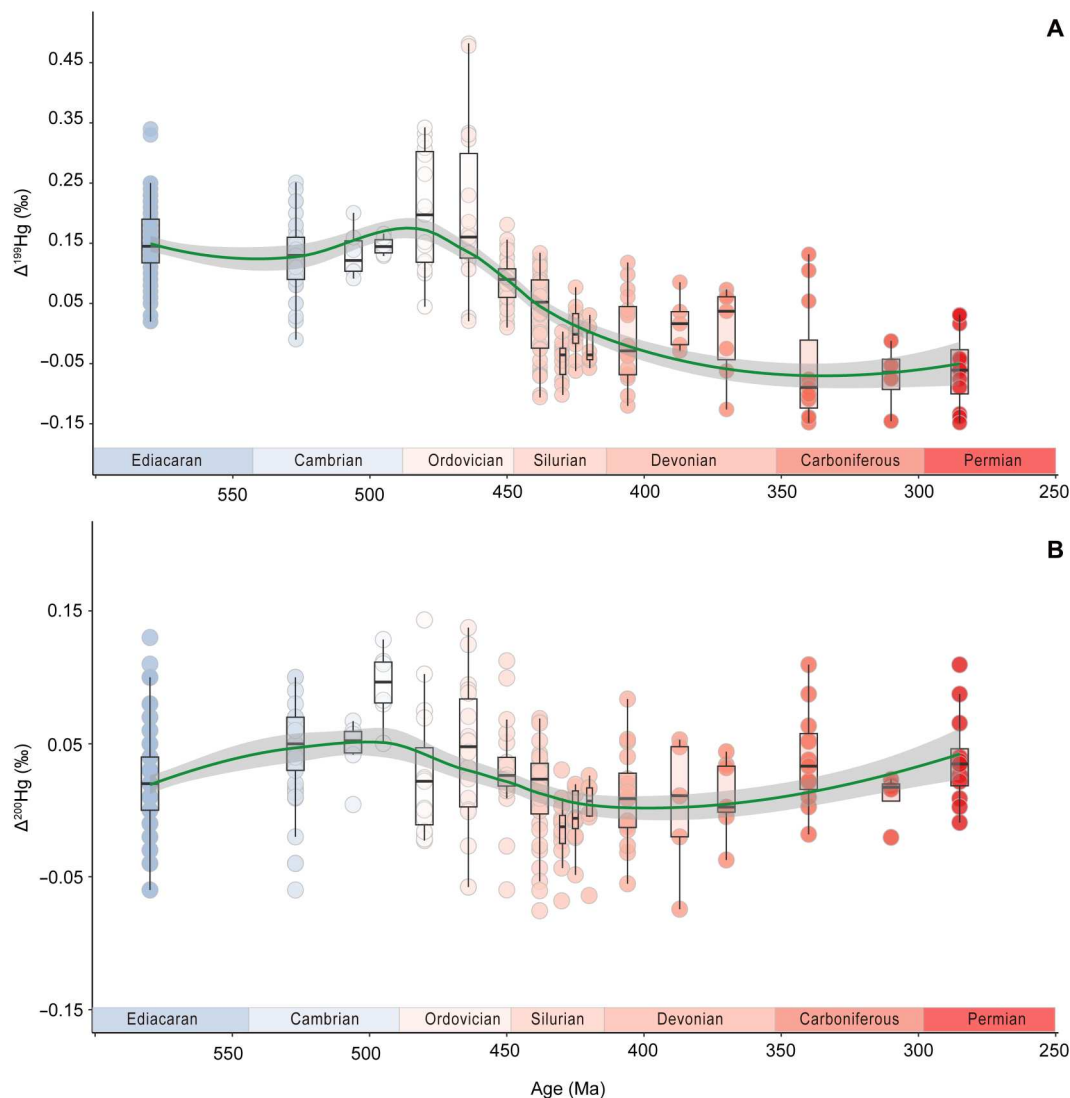


Fig. 3. Hg stable isotope composition of Paleozoic sediments in stage level ($n = 367$). A compilation of (A) $\Delta^{199}\text{Hg}$ and (B) $\Delta^{200}\text{Hg}$ ($n = 367$) of Paleozoic sediments in stage level. The green solid curve denotes a LOESS fit of the mean of the data with the 95% confidence level (gray shadow area). For the LOESS fit, the span of 0.60 is chosen based on the 10-fold cross-validation in fig. S4. In detail, the lithology and Hg isotopic data from 181 samples presented in this study along with previously published data are available in data file S1.

$\Delta^{200}\text{Hg} = 0.04 \pm 0.06\text{‰}$ ($n = 18$) (Figs. 2 and 3, A and B). The slightly negative odd-MIF signature ($P = 0.43$ by Independent t test) in Ediacaran and Cambrian is speculated to strengthening continental weathering, which is also evidenced by the higher $^{87}\text{Sr}/^{86}\text{Sr}$ values. Modeling results suggest a negligible contribution from land plants, consistent with the contemporaneous low atmospheric O_2 ($p\text{O}_2$) levels from the Cambrian to Ordovician (Fig. 4, B and F). The diversification of marine invertebrates and other microorganisms during the Early Cambrian and Ordovician did not induce a secular Hg isotope shift in marine sediments, implying that most marine life inherited the Hg isotope signature of seawater. The first tetrahedral microfossils suggest that the emergence of land plants did not occur until the Tremadocian (Early Ordovician) (19). Accordingly, it is widely assumed that before the Ordovician, microorganisms dominated the terrestrial ecosystems rather than land plants. Experimental studies, however, indicate that MIF

does not arise during the microbial cycling of Hg [(11) and references therein], congruently accounting for the higher $\Delta^{199}\text{Hg}$ values of terrestrial sources than those of present.

The interval from the Late Ordovician to Silurian is marked by the onset of a significant negative Hg MIF excursion observed in a population of 100 Hg isotope data points ($\Delta^{199}\text{Hg} = 0.01 \pm 0.07\text{‰}$ and $\Delta^{200}\text{Hg} = 0.01 \pm 0.03\text{‰}$, $n = 100$; $P < 0.01$ by Independent t test). We interpret this MIF signature as being related to the rapid colonization and subsequent expansion of land plants. In contrast to vascular plants, the nonvascular plants, mostly mosses and other cryptogamic organisms without root systems or thick, waxy cuticles, grow and produce biomass slowly due to a longer phenological cycle. Previous investigations have demonstrated that the predecessors of modern bryophytes (nonvascular plants) greatly shaped the past climate and atmosphere (1, 20, 21) and increased global chemical weathering before the Late Ordovician (22). The Hg isotope

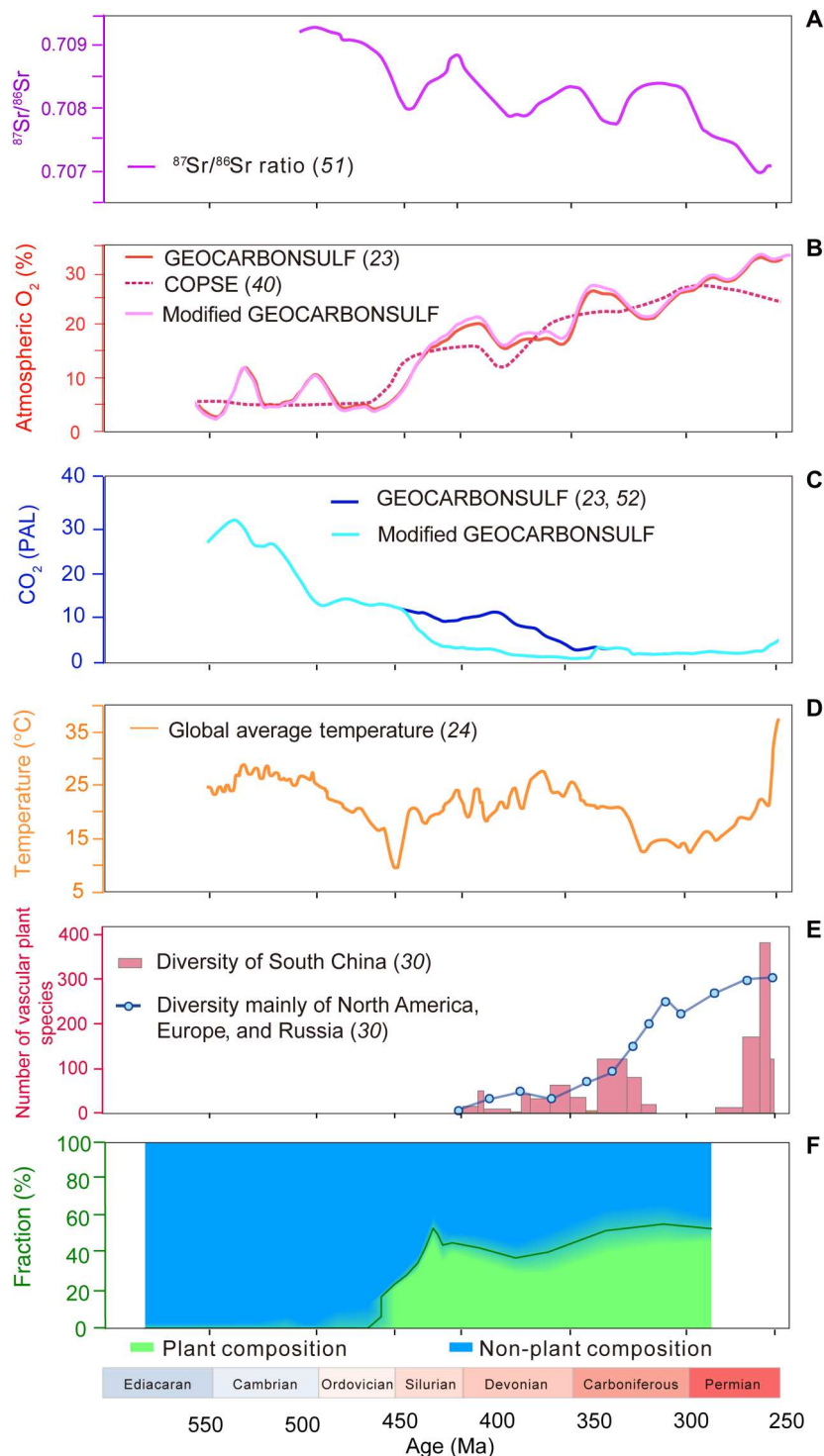


Fig. 4. Critical records in Paleozoic sediments in stage/age level. (A) $^{87}\text{Sr}/^{86}\text{Sr}$ values (in purple solid line) (51). (B) Atmospheric $p\text{O}_2$ [unit: %, in red solid line (23), dashed line (40), and pink solid line is modified GEOCARBONSULF]. (C) $p\text{CO}_2$ [unit: Present Atmospheric Level (PAL); blue solid line (23, 52), and cyan solid line is the modified GEOCARBONSULF]. (D) Global average temperature ($^{\circ}\text{C}$; in orange solid line) (24). (E) Vascular plant diversity recorded from South China and other areas, modified by Xue *et al.* (30). (F) Numerical model results of two end-member Hg isotopic model. The green solid curve denotes the mean value with the 95% confidence level (gradient shadow area).

curve, however, does not show a decreasing trend before the Late Ordovician, indicating that, although their biomass may have been three times larger than today (21, 22), the weathering flux resulting from nonvascular plant activity did not affect the Hg MIF signature observed in marine sediments. Moreover, Hg in modern mosses is not solely derived from atmospheric Hg⁰ (76%), and their perennating features and lower growth rates limit biomass production relative to those of vascular plants. Therefore, we do not attribute the distinct decreasing odd-MIF trend merely to nonvascular plants. In contrast, their shorter phenological cycle likely enabled vascular plants to transfer atmospheric Hg⁰ into terrestrial reservoirs more efficiently with distinctive negative odd- and even-MIF signatures, causing the sharp decline in MIF values from the Late Ordovician to Silurian. Furthermore, early vascular plants likely had more efficient water transport and storage abilities than nonvascular plants, and clonal growth in tangled colonies enhanced the local and, eventually the global, hydrological cycle. As vascular plants expanded into a variety of terrestrial niches, they actively altered the Hg isotope in proximal marine sediments during this episode, and there is a contemporaneous increase of pO_2 , decrease of pCO_2 , and global cooling (23, 24). The conventional view is that these positive feedbacks led to increasingly complex terrestrial ecosystems such that by the Late Devonian the evolution of full forest ecosystems resulted in, for the first time in Earth's history, an interplay between biosphere, hydrosphere, and atmosphere similar to that is experienced today (25). The data we present here suggest that such a level of global system modernization may have begun somewhat earlier in the Silurian. Similar conclusions are also suggested by the isotopic signatures of zircon formed at subduction zones where marine sediments are transported into the mantle (26), and the Fast Land Occupancy and Reaction Algorithm model (21), which consistently suggests an earlier expansion of land plants with an early peak in potential biomass at around 470 million years (Ma). Moreover, an upsurge in the proportion of mud on land was constrained to the Ordovician-Silurian, further supporting the expansion of vegetation on land (27), although the contribution of embryophytes is not fully understood. If our interpretations stand, then it is possible that these pioneer vascular plant ancestors during Ordovician-Silurian had not yet develop sizable root systems to retain fine sediments on alluvial plains, as the abundance of lateral accretion sets of meandering rivers did not increase globally until the late Silurian (28).

The Devonian experienced a mildly contracted terrestrial biomass according to the model, in parallel with fluctuating pO_2 and global temperature (Fig. 4, B and C). Although some studies have emphasized global ocean oxygenation during the Devonian (29), both GEOCARBONSULF and COPSE models demonstrate a decreasing atmospheric pO_2 trend in the Early Devonian; although small in magnitude, it is possibly attributable to variations in land plant biomass. From the Carboniferous to the early Permian, the distinct negative odd-MIF ($\Delta^{199}\text{Hg} = -0.06 \pm 0.07\text{‰}$ and $\Delta^{200}\text{Hg} = 0.03 \pm 0.03\text{‰}$, $n = 27$) implies that the negative end member induced by terrestrial Hg sources played a dominant role in Hg accumulation and contributed up to 53 to 56% of total Hg input. This is consistent with land plant species diversification and increase in terrestrial biomass (30), which are supported by the highest pO_2 and lowest global temperature estimates during the Paleozoic (Fig. 4, B and D) (31). In particular, the major geographic expansion of seed plant floras with well-developed deeper root systems may have

considerably enhanced chemical and physical weathering (32), thus increasing Hg release from terrigenous sources.

DISCUSSION

An earlier evolution of vascular plants

Our data demonstrate that land plants profoundly affected terrestrial ecosystems as early as the Ordovician-Silurian transition, although few contemporaneous vascular plant megafossils were reported for that time (Fig. 4E) (30, 33). The evolution of plant vascularization has been considered as an extremely slow process. Those earliest land inhabitants lived in tangled clonal communities, which enabled a humid microclimate to develop between the stems and raised the boundary layer (a relatively still and humid layer of air above to the ground). Their subsequent growing height to release spores into the air above the boundary layer could have led to increase in stature and greater vascularization (34). On the basis of fossil records (Fig. 4E), the Devonian Plant Hypothesis (DPH) suggests that the rapid development of root systems, deep ploughing of soils, and enhancement of the hydrological cycle by vascular plants did not occur until the Devonian. These processes consistently enabled the terrestrial plants to expand dominantly on land, which fundamentally reshaped Earth's landforms physically and chemically (35). In the absence of deep rooting systems, the early terrestrial ecosystems may have resulted in drier, shallower, and less stable soil ecosystems with lower productivity, in contrast to those of today (36), which resulted in a dearth of alluvial facies conducive to fossilizing vascular plants before the Devonian (37). The presence of land plant body fossils is highly sensitive to facies type, where they are usually abundant in fluvial or lacustrine settings. This suggests that the enhanced development and preservation of terrestrial sediments during the Devonian Period is likely to be an overriding factor controlling the appearance and abundance of plant body fossils, which potentially resulted in limited preservation of pre-Devonian terrestrial macrofossils, and therefore our ability to study these environments. According to the DPH, although the earliest vascular plant fossils (Cooksonia) have been identified in Silurian (Wenlock) strata (38), it is not convincing to link the sparse presence of this earliest vascular plant fossil with large-scale reshaping of Earth's terrestrial systems. Trilete spores, which are dominantly produced by vascular plants today, occur in the lower Upper Ordovician Sandbian strata (458.4 to 453.0 Ma) and may push the origin of vascular plants earlier to the Late Ordovician (33). A Bayesian-related molecular clock calculation based on phylogenomic data encompassing the diversity of surviving embryophytes suggests that land plant clades first appeared in the Middle Cambrian–Early Ordovician, and the origin of vascular plants occurred in the Late Ordovician (4). This suggests that vascular plants may have prevailed on land during the Late Ordovician–Silurian interval. Our Hg isotope data are consistent with the hypothesis that land was extensively greened and shaped by vascular ground-hugging plants before the Devonian, although they likely had small and simple root-like structures. To produce an indelible mark on the Hg signature of marine sediments, these terrestrial pioneers must have been widely distributed, at least in coastal and riparian zones at lower latitudes such as in South China (39).

Profound impact on the atmosphere and surface of Earth

Despite some differences in the estimation of absolute oxygen content, both COPSE (40) and GEOCARBONSULF (23) models suggest two episodes of distinct increase of atmospheric pO_2 ; one was from the Ordovician to the end of the Silurian, and the other was from the Late Devonian to Permian (Fig. 4B). These atmospheric oxygenation events are temporally correlated with both the diversification and expansion of vascular plants on land and agree with our interpretation of the Hg isotope datasets. In addition to photosynthesis, vascular plants also play an important role in affecting the chemical weathering of silicate rocks—another principal sink of atmospheric CO_2 over geologic time (41). We have revised the parameters in the GEOCARBONSULF model, assuming that the vascular plants had colonized land extensively at ~444 Ma to reconstruct atmospheric O_2 and CO_2 concentrations (Fig. 4, B and C). The modified atmospheric O_2 record shows similar estimations with and slightly higher than that in the original curve. In contrast, the decreasing trend from ~15 to 3 Present Atmospheric Level (PAL) of CO_2 during Devonian-Carboniferous in the original model occurred earlier in the Silurian in the revised model. We highlight that vascular plant expansion would decrease atmospheric CO_2 concentrations rapidly, and we encourage future research to test these conclusions. Unlike the lower plants, vascular plants are characterized by lignin-related tissues rich in various refractory organic compounds in which the Carbon(C): Phosphorus (P) ratio is four-fold that of marine organic matter (42). The emergence and expansion of peroxidase enzymes needed for lignin decomposition did not begin until the diversification of Basidiomycota during the early Permian, approximately 295 Ma ago (43). In this light, a secular carbon sequestration process maintained by early colonization of land plants could have profoundly shaped atmospheric chemistry. Consequently, these factors would contribute to an increase in terrestrial sediment fluxes and likely organic carbon burial rates in marine basins over long time scales.

The persistent removal of carbon from the ocean-atmosphere system also affects oxygen levels. The photolysis of CO_2 during photosynthesis produces organic carbon and oxygen, and if the carbon is buried as organic matter in sediments, then oxygen builds up in the atmosphere, sustaining the secular rise of atmospheric pO_2 levels. The reservoir of a substantial organic carbon pool stabilized the atmosphere at a higher oxygen level, ultimately altering our planet's redox history. This paved the way for the evolution of large, mobile animals that have dominated the Earth's surface since the Middle Paleozoic (41).

The seawater $^{87}Sr/^{86}Sr$ curve can be dominantly affected by the relative contribution of the weathering of continental crust (~0.711 or higher) and input via seafloor hydrothermal systems (~0.704). The Silurian Period is characterized by increasing $^{87}Sr/^{86}Sr$ values, suggesting progressively enhanced terrestrial weathering of continental crust or attenuated oceanic ridge activity coincident with the first episode of land plant expansion as observed in South China and peripheral continents. As plants spread across the land, they enhanced weathering and grew to taller heights, thereby elevating terrestrial biomass and organic input to the oceans. The secular variation of the seawater $^{87}Sr/^{86}Sr$ record, however, cannot be attributed solely to land plant colonization, as tectonic activity can also contribute. Moreover, although these early plants can effectively increase the local weathering intensity, it is still extremely difficult for them to extend into most regions of the

continental interior due to their primitive water-retaining structures. Therefore, it is very likely that tectonic activity remains the primary controlling factor for the Early Paleozoic secular seawater $^{87}Sr/^{86}Sr$ curve. The variation in the seawater $^{87}Sr/^{86}Sr$ curve is decoupled from the land plants expansion that took place in the Carboniferous, possibly due to the progressive amalgamation of the supercontinent Pangea. The two episodes of land plant expansion during the Paleozoic illustrated by the two end-member Hg isotopic models also coincide with global cooling (Fig. 4, D and F). The first occurred during the Ordovician-Silurian transition, highlighted by the Late Ordovician (Hirnantian) glaciation event and potentially related to the emergence and expansion of the earliest plants (20). The second occurred during the Devonian-Carboniferous transition, broadly coincident with the Late Paleozoic Ice Age, possibly driven by expansion of seed plants (44, 45). These findings demonstrate the intimate relationships between the coevolution of land plants, global climate, and Earth surface systems.

MATERIALS AND METHODS

Sampling

In this study, the data are mostly based on classical stratotype profiles or profiles with a well-established bottom framework, which can substantially reduce the stratigraphic uncertainties. The sampling sites are illustrated in fig. S1 using modern geography, while the detailed data from different geological periods are presented in section S1. Mercury is transported to deep-water settings predominantly through the atmosphere and to shallow-water settings via riverine runoff. Thus, intensified chemical weathering and subsequent increase in terrestrial input to the oceans may consequently decrease $\Delta^{199}Hg$ values in marine sediments (9). The expanded numbers of samples, including data compiled from previous publications (367 samples in total, which are detailed in data file S1, where 181 samples collected on the published stratigraphic sections are measured in this study) cover different lithologies and sedimentary facies and reduce the facies bias on Hg isotopes. The depositional facies were simplified into deep- and shallow-water settings based on the grain sizes and the relatively content of carbonate minerals (see lithological descriptions and photos in the Supplementary Materials). The deep- and shallow-water depositional facies show negligible differences in Hg isotopes (Fig. 5). In addition, to prevent potential overprinting from excessive volcanic source loading over the bulk Hg isotopic signals in sedimentary rocks, we selected samples that are not associated with volcanic ash layers to avoid intervals that are possibly subjected to the effects of LIP activity (8). Sediments deposited across major biotic events associated with large-scale volcanism were also excluded when evaluating terrigenous input. Therefore, data from the Permian Guadalupian and Lopingian stages were not included in this compilation due to the unequivocal geological evidence of the Emeishan LIP and Siberia LIP emplacements (46). As shown in Fig. 1, the Hg^{II} in liquid phase can be dominantly reduced to Hg^0 induced by photoreduction, resulting in positive $\Delta^{199}Hg$ in residual Hg^{II} deposited into ocean sediments. These distinct positive $\Delta^{199}Hg$ values were evident in pre-Cambrian sediments with ~0.20‰. We also note that some negative $\Delta^{199}Hg$ values have been reported in pre-Cambrian intervals, such as sulfur-bound Hg reduction in euxinic environments (10), ancient metamorphic rocks (47), and samples associated with subaerial volcanism (48). These particular events

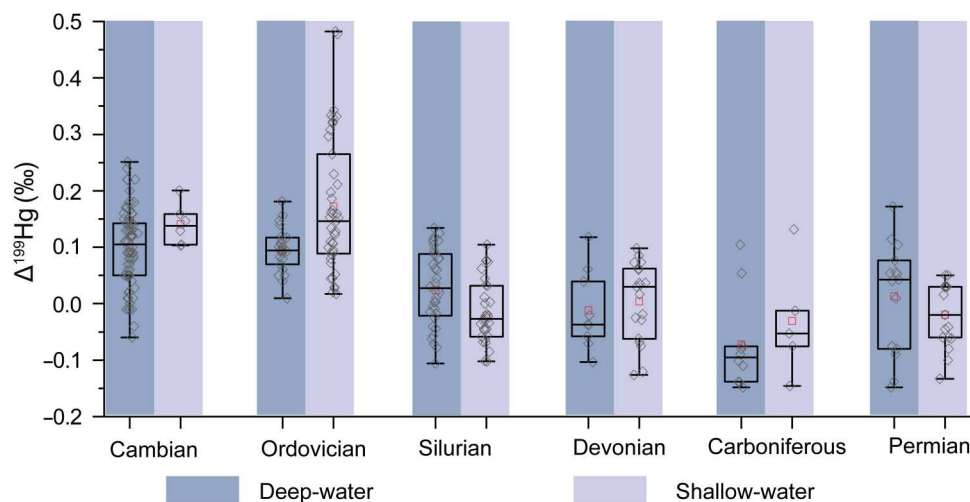


Fig. 5. Comparison between the Hg isotope odd-MIF signature in different deposition environment. The sample deposition environment include shallow-water (limestone, dolostone, and sandstone; in light shade) and deep-water (shale and chert) (in dark shade) settings in each period for the Paleozoic.

only reflect a unique depositional environment under which the Hg isotopic values were not included in the present compilation.

Hg concentration and isotope measurement

We dug the fresh rock samples, trim them to remove visible veins and weathered surfaces, and cleaned in double-distilled water in sequence. Crusts and veins were cautiously avoided before obtaining the powders from hand specimen samples after petrographic examination. We offer petrographic evidences to show that Hg in rock samples can represent the syndepositional Hg stable isotopic characteristics without contamination by younger material (section S2). First, the sedimentary rock samples are typified with horizontal beddings and primary sedimentary structures. Moreover, the absence of diagenetic minerals, such as hematite, indicates that the diagenesis is not the primary control of geochemical signals. In addition, the intact crystal shape of diagenetic minerals without recrystallization suggests inessential postsedimentary processes, such as hydrothermal vein metasomatism or superposition. After drying treatment, all rock samples were ground into power and sieved with a 200-mesh (74 μm) nylon screen, which aimed to mix the sample evenly and reduce the heterogeneity. The samples were analyzed for their respective Hg concentration and isotope compositions. Both Hg concentration and isotope compositions were measured at the State Key Laboratory of Environmental Geochemistry, Institute of Geochemistry, Chinese Academy of Sciences, Guiyang. The total Hg concentration was determined using a Direct Mercury Analyzer (DMA-80, Italy). One replicate sample was analyzed for every nine samples, and certified soil reference material GBW 07405 ($290 \pm 30 \text{ ng g}^{-1}$) was analyzed for every 10 samples with 90 to 105% recovery.

The preconcentration of rock samples with low Hg (calculated as $\sim 10 \text{ ng Hg}$) were completed by the double-stage heating pyrolysis combustion of tube muffle furnace with pure oxygen gas flows (25 ml min^{-1}). Oidizing solution (5 ml) of 40% mixture of nitric and hydrochloric acid [“reverse aqua regia”, $\text{HNO}_3:\text{HCl} = 2:1$ (v/v)] was used as trapping solution to capture Hg^0 vapor. The preconcentration recovery was determined to be $97.2 \pm 6.5\%$ ($n = 18, \pm 1\sigma$)

by using soil certified reference materials (GSS-4; with a total Hg concentration of $590 \pm 50 \text{ ng g}^{-1}$).

Mercury isotopes were measured by multicollector inductively coupled plasma mass spectrometer (Neptune II, Thermo Fisher Scientific, USA). The sample solution was diluted to 0.5 ng g^{-1} (10% acidity) and was then reduced by 3% SnCl_2 to Hg^0 in an online Hg vapor generation system (17). The Tl standard (NIST SRM 997) was used as an internal standard, and an Hg standard [National Institute of Standards and Technology (NIST) Standard Reference Material (SRM) 3133] was used as an external standard sample. Hg isotope data are reported relative to NIST-3133 for MDF as follows

$$\delta^{202}\text{Hg}(\text{‰}) = \left[\frac{(^{202}\text{Hg}/^{198}\text{Hg})_{\text{sample}}}{(^{202}\text{Hg}/^{198}\text{Hg})_{\text{NIST-3133}}} - 1 \right] \times 1000 \quad (3)$$

MIF is calculated as

$$\Delta^{xxx}\text{Hg} = \delta^{xxx}\text{Hg} - \beta_{xxx} \times \delta^{202}\text{Hg} \quad (4)$$

where β_{xxx} is 0.252 for ^{199}Hg , 0.502 for ^{200}Hg , and 0.752 for ^{201}Hg , respectively (49).

NIST-8610 (UM-Almadén) was measured every 10 to 15 samples during isotope measurement as a secondary standard to confirm the accuracy and precision of measurements. Results of NIST-8610 ($\delta^{202}\text{Hg} = -0.54 \pm 0.09\text{‰}$, $\Delta^{199}\text{Hg} = -0.01 \pm 0.06\text{‰}$, $\Delta^{200}\text{Hg} = 0.01 \pm 0.05\text{‰}$, and $\Delta^{201}\text{Hg} = -0.03 \pm 0.07\text{‰}$; $\pm 2\text{SD}$, $n = 30$) and GSS-4 ($\delta^{202}\text{Hg} = -1.79 \pm 0.12\text{‰}$, $\Delta^{199}\text{Hg} = -0.40 \pm 0.09\text{‰}$, $\Delta^{200}\text{Hg} = -0.01 \pm 0.05\text{‰}$, and $\Delta^{201}\text{Hg} = -0.38 \pm 0.08\text{‰}$; $\pm 2\text{SD}$, $n = 18$) are consistent with the recommended values (50), suggesting that our preconcentration did not induce extra uncertainties.

Supplementary Materials

This PDF file includes:

Figs. S1 to S12

Table S1

Sections S1 to S3

References

Other Supplementary Material for this manuscript includes the following:

R code

Supplementary material_Hg isotope data available_Data S1

REFERENCES AND NOTES

1. T. M. Lenton, T. W. Dahl, S. J. Daines, B. J. Mills, K. Ozaki, M. R. Saltzman, P. Porada, Earliest land plants created modern levels of atmospheric oxygen. *Proc. Natl. Acad. Sci. U.S.A.* **113**, 9704–9709 (2016).
2. M. R. Gibling, N. S. Davies, Palaeozoic landscapes shaped by plant evolution. *Nat. Geosci.* **5**, 99–105 (2012).
3. P. Gerrienne, T. Servais, M. Vecoli, Plant evolution and terrestrialization during Palaeozoic times—The phylogenetic context. *Rev. Palaeobot. Palynol.* **227**, 4–18 (2016).
4. J. L. Morris, M. N. Puttick, J. W. Clark, D. Edwards, P. Kenrick, S. Pressel, C. H. Wellman, Z. Yang, H. Schneider, P. C. J. Donoghue, The timescale of early land plant evolution. *Proc. Natl. Acad. Sci. U.S.A.* **115**, E2274–E2283 (2018).
5. A. M. F. Tomescu, Mysteries of the bryophyte tracheophyte transition revealed enter the eophytes. *New Phytol.* **233**, 1018–1021 (2022).
6. P. Kenrick, C. H. Wellman, H. Schneider, G. D. Edgecombe, A timeline for terrestrialization: Consequences for the carbon cycle in the Palaeozoic. *Philos. Trans. R. Soc. Lond. B Biol. Sci.* **367**, 519–536 (2012).
7. T. Servais, B. Cascales-Miñana, C. J. Cleal, P. Gerrienne, D. A. T. Harper, M. Neumann, Revisiting the Great Ordovician Diversification of land plants: Recent data and perspectives. *Palaeogeogr. Palaeoclimatol. Palaeoecol.* **534**, 109280 (2019).
8. S. E. Grasby, T. R. Them, Z. Chen, R. Yin, O. H. Ardakani, Mercury as a proxy for volcanic emissions in the geologic record. *Earth Sci. Rev.* **196**, 102880 (2019).
9. T. R. Them, C. H. Jagoe, A. H. Caruthers, B. C. Gill, S. E. Grasby, D. R. Gröcke, R. Yin, J. D. Owens, Terrestrial sources as the primary delivery mechanism of mercury to the oceans across the Toarcian Oceanic Anoxic Event (Early Jurassic). *Earth Planet. Sci. Lett.* **507**, 62–72 (2019).
10. W. Zheng, G. J. Gilleaudeau, L. C. Kah, A. D. Anbar, Mercury isotope signatures record photic zone euxinia in the Mesoproterozoic ocean. *Proc. Natl. Acad. Sci. U.S.A.* **115**, 10594–10599 (2018).
11. J. D. Blum, L. S. Sherman, M. W. Johnson, Mercury isotopes in earth and environmental sciences. *Annu. Rev. Earth Planet. Sci.* **42**, 249–269 (2014).
12. M. Jiskra, L. E. Heimbürger-Boavida, M. M. Desgranges, M. V. Petrova, A. Dufour, B. Ferreira-Araujo, J. Masbou, J. Chmeleff, M. Thyssen, D. Point, J. E. Sonke, Mercury stable isotopes constrain atmospheric sources to the ocean. *Nature* **597**, 678–682 (2021).
13. Z. Liu, H. Tian, R. Yin, D. Chen, H. Gai, Mercury loss and isotope fractionation during thermal maturation of organic-rich mudrocks. *Chem. Geol.* **612**, 121144 (2022).
14. D. Chen, D. Ren, C. Deng, Z. Tian, R. Yin, Mercury loss and isotope fractionation during high-pressure and high-temperature processing of sediments: Implication for the behaviors of mercury during metamorphism. *Geochim. Cosmochim. Acta* **334**, 231–240 (2022).
15. J. Zhou, D. Obrist, Global mercury assimilation by vegetation. *Environ. Sci. Technol.* **55**, 14245–14257 (2021).
16. P. M. Outridge, R. P. Mason, F. Wang, S. Guerrero, L. E. Heimbürger-Boavida, Updated global and oceanic mercury budgets for the United Nations Global Mercury Assessment 2018. *Environ. Sci. Technol.* **52**, 11466–11477 (2018).
17. X. Wang, W. Yuan, C.-J. Lin, X. Feng, Mercury cycling and isotopic fractionation in global forests. *Crit. Rev. Environ. Sci. Technol.* **52**, 3763–3786 (2022).
18. L. C. Motta, L. Kritee, J. D. Blum, M. Tsz-Ki Tusi, J. R. Reinfelder, Mercury Isotope Fractionation during the Photochemical Reduction of Hg(II) Coordinated with Organic Ligands. *J. Phys. Chem. A* **124**, 2842–2853 (2020).
19. P. K. Strother, C. Foster, A fossil record of land plant origins from charophyte algae. *Science* **373**, 792–796 (2021).
20. T. M. Lenton, M. Crouch, M. Johnson, N. Pires, L. Dolan, First plants cooled the Ordovician. *Nat. Geosci.* **5**, 86–89 (2012).
21. K. Gurlung, K. J. Field, S. A. Batterman, Y. Godderis, Y. Donnadieu, P. Porada, L. L. Taylor, B. J. W. Mills, Climate windows of opportunity for plant expansion during the Phanerozoic. *Nat. Commun.* **13**, 4530 (2022).
22. P. Porada, T. M. Lenton, A. Pohl, B. Weber, L. Mander, Y. Donnadieu, C. Beer, U. Poschl, A. Kleidon, High potential for weathering and climate effects of non-vascular vegetation in the Late Ordovician. *Nat. Commun.* **7**, 12113 (2016).
23. A. J. Krause, B. J. W. Mills, S. Zhang, N. J. Planavsky, T. M. Lenton, S. W. Poulton, Stepwise oxygenation of the Paleozoic atmosphere. *Nat. Commun.* **9**, 4081 (2018).
24. C. R. Scotese, H. Song, B. J. Mills, D. van der Meer, Phanerozoic paleotemperatures: The earth's changing climate during the last 540 million years. *Earth Sci. Rev.* **215**, 103503 (2021).
25. R. A. Spicer, Physiological characteristics of land plants in relation to environment through time. *Trans. R. Soc. Edinb. Earth Sci.* **80**, 321–329 (1989).
26. C. J. Spencer, N. S. Davies, T. M. Gernon, X. Wang, W. J. McMahon, T. R. I. Morrell, T. Hincks, P. K. Pufahl, A. Brasier, M. Seraine, G.-M. Lu, Composition of continental crust altered by the emergence of land plants. *Nat. Geosci.* **15**, 735–740 (2022).
27. W. J. McMahon, N. S. Davies, Evolution of alluvial mudrock forced by early land plants. *Science* **359**, 1022–1024 (2018).
28. N. S. Davies, M. R. Gibling, Cambrian to Devonian evolution of alluvial systems: The sedimentological impact of the earliest land plants. *Earth Sci. Rev.* **98**, 171–200 (2010).
29. T. W. Dahl, E. U. Hammarlund, A. D. Anbar, D. P. Bond, B. C. Gill, G. W. Gordon, A. H. Knoll, A. T. Nielsen, N. H. Schovsbo, D. E. Canfield, Devonian rise in atmospheric oxygen correlated to the radiations of terrestrial plants and large predatory fish. *Proc. Natl. Acad. Sci. U.S.A.* **107**, 17911–17915 (2010).
30. J. Xue, P. Huang, M. Ruta, M. J. Benton, S. Hao, C. Xiong, D. Wang, B. Cascales-Miñana, Q. Wang, L. Liu, Stepwise evolution of Paleozoic tracheophytes from South China: Contrasting leaf disparity and taxic diversity. *Earth Sci. Rev.* **148**, 77–93 (2015).
31. D. J. Beerling, R. A. Berner, Impact of a Permo-Carboniferous high O₂ event on the terrestrial carbon cycle. *Proc. Natl. Acad. Sci. U.S.A.* **97**, 12428–12432 (2000).
32. J. Quirk, J. R. Leake, D. A. Johnson, L. L. Taylor, L. Saccone, D. J. Beerling, Constraining the role of early land plants in Palaeozoic weathering and global cooling. *Proc. Biol. Sci.* **282**, 20151115 (2015).
33. C. V. Rubinstein, V. Vajda, Baltica cradle of early land plants? Oldest record of trilete spores and diverse cryptospore assemblages; evidence from Ordovician successions of Sweden. *GFF* **141**, 181–190 (2019).
34. C. J. Harrison, J. L. Morris, The origin and early evolution of vascular plant shoots and leaves. *Philos. Trans. R Soc. B* **373**, 20160496 (2018).
35. J. Xue, Z. Deng, P. Huang, K. Huang, M. J. Benton, Y. Cui, D. Wang, J. Liu, B. Shen, J. F. Basinger, S. Hao, Belowground rhizomes in paleosols: The hidden half of an Early Devonian vascular plant. *Proc. Natl. Acad. Sci. U.S.A.* **113**, 9451–9456 (2016).
36. T. W. Dahl, S. K. M. Arens, The impacts of land plant evolution on Earth's climate and oxygenation state – An interdisciplinary review. *Chem. Geol.* **547**, 119665 (2020).
37. A. Smith, A. J. McGowan, The shape of the Phanerozoic marine palaeodiversity Curve: How much can be predicted from the sedimentary rock record of Western Europe? *Palaeontology* **50**, 765–774 (2007).
38. M. Libertin, J. Kvacek, J. Bek, V. Zarsky, P. Storch, Sporophytes of polysporangiate land plants from the early Silurian period may have been photosynthetically autonomous. *Nat. Plants* **4**, 269–271 (2018).
39. J. Xue, P. Huang, D. Wang, C. Xiong, L. Liu, J. F. Basinger, Silurian-Devonian terrestrial revolution in South China: Taxonomy, diversity, and character evolution of vascular plants in a paleogeographically isolated, low-latitude region. *Earth Sci. Rev.* **180**, 92–125 (2018).
40. T. M. Lenton, S. J. Daines, B. J. W. Mills, COPSE reloaded: An improved model of biogeochemical cycling over Phanerozoic time. *Earth Sci. Rev.* **178**, 1–28 (2018).
41. R. A. Berner, Phanerozoic atmospheric oxygen: New results using the GEOCARBSULF model. *Am. J. Sci.* **309**, 603–606 (2009).
42. N. M. Bergman, T. M. Lenton, A. J. Watson, COPSE: A new model of biogeochemical cycling over Phanerozoic time. *Am. J. Sci.* **304**, 397–437 (2004).
43. M. L. Berbee, C. Strullu-Derrien, P. M. Delaux, P. K. Strother, P. Kenrick, M. A. Selosse, J. W. Taylor, Genomic and fossil windows into the secret lives of the most ancient fungi. *Nat. Rev. Microbiol.* **18**, 717–730 (2020).
44. C. K. Boyce, J.-E. Lee, Plant evolution and climate over geological timescales. *Annu. Rev. Earth Planet. Sci.* **45**, 61–87 (2017).
45. B. Chen, J. Chen, W. Qie, P. Huang, T. He, M. M. Joachimski, M. Regelous, P. A. E. Pogge von Strandmann, J. Liu, X. Wang, I. P. Montañez, T. J. Algeo, Was climatic cooling during the earliest Carboniferous driven by expansion of seed plants? *Earth Planet. Sci. Lett.* **565**, 116953 (2021).
46. P. B. Wignall, Y. Sun, D. P. Bond, G. Izon, R. J. Newton, S. Vedrine, M. Widdowson, J. R. Ali, X. Lai, H. Jiang, H. Cope, S. H. Bottrell, Volcanism, mass extinction, and carbon isotope fluctuations in the Middle Permian of China. *Science* **324**, 1179–1182 (2009).
47. C. Deng, J. Zhang, R. Hu, K. Luo, Y. Zhu, R. Yin, Mercury isotope constraints on the genesis of late Mesozoic Sb deposits in South China. *Sci. China Earth Sci.* **65**, 269–281 (2022).
48. J. Meixnerova, J. D. Blum, M. W. Johnson, E. E. Stueken, M. A. Kipp, A. D. Anbar, R. Buick, Mercury abundance and isotopic composition indicate subaerial volcanism prior to the end-Archean "whiff" of oxygen. *Proc. Natl. Acad. Sci. U.S.A.* **118**, e2107511118 (2021).
49. B. A. Bergquist, J. D. Blum, Mass-dependent and -Independent fractionation of Hg isotopes by photoreduction in aquatic systems. *Science* **318**, 417–420 (2007).
50. J. D. Blum, M. W. Johnson, Recent developments in mercury stable isotope analysis. *Rev. Mineral. Geochem.* **82**, 733–757 (2017).
51. J. M. McArthur, R. J. Howarth, G. A. Shields, Y. Zhou, Chapter 7 - Strontium isotope stratigraphy. *Geol. Time Scale 2020* **1**, 211–238 (2020).

52. D. L. Royer, Y. Donnadieu, J. Park, J. Kowalczyk, Y. Godderis, Error analysis of CO₂ and O₂ estimates from the long-term geochemical model GEOCARBSULF. *Am. J. Sci.* **314**, 1259–1283 (2014).
53. H. Zhao, J. Shen, T. J. Algeo, G. Racki, J. Chen, C. Huang, J. Song, W. Qie, Y. Gong, Mercury isotope evidence for regional volcanism during the Frasnian-Famennian transition. *Earth Planet. Sci. Lett.* **581**, 117412 (2022).
54. Y. Huang, Z.-Q. Chen, P. B. Wignall, S. E. Grasby, L. Zhao, X. Wang, K. Kaiho, Biotic responses to volatile volcanism and environmental stresses over the Guadalupian-Lopingian (Permian) transition. *Geology* **47**, 175–178 (2018).
55. J. Shen, J. Chen, T. J. Algeo, Q. Feng, J. Yu, Y.-G. Xu, G. Xu, Y. Lei, N. J. Planavsky, S. Xie, Mercury fluxes record regional volcanism in the South China craton prior to the end-Permian mass extinction. *Geology* **49**, 452–456 (2020).
56. Q. Gong, X. Wang, L. Zhao, S. E. Grasby, Z. Q. Chen, L. Zhang, Y. Li, L. Cao, Z. Li, Mercury spikes suggest volcanic driver of the Ordovician-Silurian mass extinction. *Sci. Rep.* **7**, 5304 (2017).
57. D. P. G. Bond, S. E. Grasby, Late Ordovician mass extinction caused by volcanism, warming, and anoxia, not cooling and glaciation. *Geology* **48**, 777–781 (2020).
58. J. Shen, T. J. Algeo, J. Chen, N. J. Planavsky, Q. Feng, J. Yu, J. Liu, Mercury in marine Ordovician/Silurian boundary sections of South China is sulfide-hosted and non-volcanic in origin. *Earth Planet. Sci. Lett.* **511**, 130–140 (2019).
59. C. E. Mitchell, M. J. Melchin, Late Ordovician mass extinction caused by volcanism, warming, and anoxia, not cooling and glaciation: Comment. *Geology* **48**, 777–781 (2020).
60. H. Fan, X. Fu, J. F. Ward, R. Yin, H. Wen, X. Feng, Mercury isotopes track the cause of carbon perturbations in the Ediacaran ocean. *Geology* **49**, 248–252 (2021).
61. R. Sun, J. Shen, S. E. Grasby, J. Zhang, J. Chen, C. Yang, R. Yin, CO₂ buildup drove global warming, the Marinoan deglaciation, and the genesis of the Ediacaran cap carbonates. *Precambrian Res.* **383**, 106891 (2022).
62. Z.-R. R. Liu, M.-F. Zhou, W. Wang, Mercury anomalies across the Ediacaran–Cambrian boundary: Evidence for a causal link between continental erosion and biological evolution. *Geochim. Cosmochim. Acta* **304**, 327–346 (2021).
63. R. Yin, L. Xu, B. Lehmann, R. F. Lepak, J. P. Hurley, J. Mao, X. Feng, R. Hu, Anomalous mercury enrichment in Early Cambrian black shales of South China: Mercury isotopes indicate a seawater source. *Chem. Geol.* **467**, 159–167 (2017).
64. Y. Ding, D. Chen, X. Zhou, C. Guo, T. Huang, G. Zhang, Tectono-depositional pattern and evolution of the middle Yangtze Platform (South China) during the late Ediacaran. *Precambrian Res.* **333**, 105426 (2019).
65. Y. Zhao, J. Yuan, L. E. Babcock, Q. Guo, J. Peng, L. Yin, X. Yang, S. Peng, C. Wang, R. R. Gaines, J. Esteve, T. Tai, R. Yang, Y. Wang, H. Sun, Y. Yang, Global Standard Stratotype-Section and Point (GSSP) for the conterminous base of the Miaolingian Series and Wuliuan Stage (Cambrian) at Balang, Jianhe, Guizhou, China. *Episodes* **42**, 165–184 (2019).
66. C. Xu, H. Zhong, R.-Z. Hu, H.-J. Wen, W.-G. Zhu, Z.-J. Bai, H.-F. Fan, F.-F. Li, T. Zhou, Sources and ore-forming fluid pathways of carbonate-hosted Pb–Zn deposits in Southwest China: Implications of Pb–Zn–S–Cd isotopic compositions. *Miner. Deposita* **55**, 491–513 (2020).
67. Y. Lu, T. Zhou, Trilobites across the Cambrian-Ordovician boundary of the transitional region of Sandu, Southeastern Guizhou, in *Palaeontologia Cathayana*, Y. Lu, Ed. (Springer, 1990), vol. 5, pp. 1–84.
68. T. H. Torsvik, L. R. M. Cocks, Chapter 2 New global palaeogeographical reconstructions for the Early Palaeozoic and their generation. *Geol. Soc. Publ.* **38**, 5–24 (2013).
69. C. Guo, D. Chen, Y. Song, X. Zhou, Y. Ding, G. Zhang, Depositional environments and cyclicity of the Early Ordovician carbonate ramp in the western Tarim Basin (NW China). *J. Asian Earth Sci.* **158**, 29–48 (2018).
70. M. Liu, D. Chen, X. Zhou, W. Yuan, M. Jiang, L. Liu, Climatic and oceanic changes during the Middle-Late Ordovician transition in the Tarim Basin, NW China and implications for the Great Ordovician Biodiversification Event. *Palaeogeogr. Palaeoclimatol. Palaeoecol.* **514**, 522–535 (2019).
71. X. Yang, D. Yan, D. Chen, M. Liu, X. She, J. Zhang, X. Wei, Z. Lu, Spatial variation of carbon isotopic compositions of carbonate and organic matter from the Late Ordovician sedimentary succession in the Yangtze Platform, South China: Implications for sea – Level eustasy and shoaling of marine chemocline. *J. Asian Earth Sci.* **202**, 104540 (2020).
72. D. S. Jones, D. A. Fike, S. Finnegan, W. W. Fischer, D. P. Schrag, D. McCay, Terminal Ordovician carbon isotope stratigraphy and glacioeustatic sea-level change across Anticosti Island (Quebec, Canada). *Geol. Soc. Am. Bull.* **123**, 1645–1664 (2011).
73. M. Liu, D. Chen, L. Jiang, R. G. Stockey, D. Aseal, B. Zhang, K. Liu, X. Yang, D. Yan, N. J. Planavsky, Oceanic anoxia and extinction in the latest Ordovician. *Earth Planet. Sci. Lett.* **588**, 117553 (2022).
74. W.-J. Zhao, M. Zhu, A review of Silurian fishes from Yunnan, China and related biostratigraphy. *Palaeoworld* **24**, 243–250 (2015).
75. J. Liu, X. Ma, C. Lin, H. Yang, Z. Shu, C. Fu, L. Schulte, I. Somerville, The Silurian red beds of Tarim Basin: Signals of palaeoenvironment, palaeoclimate, and sea-level change. *Geol. J.* **55**, 3837–3856 (2020).
76. W. Qie, X. Ma, H. Xu, L. Qiao, K. Liang, W. Guo, J. Song, B. Chen, J. Lu, Devonian integrative stratigraphy and timescale of China. *Sci. China Earth Sci.* **62**, 112–134 (2019).
77. D. Chen, M. E. Tucker, The Frasnian–Famennian mass extinction: Insights from high-resolution sequence stratigraphy and cyclostratigraphy in South China. *Palaeogeogr. Palaeoclimatol. Palaeoecol.* **193**, 87–111 (2003).
78. P. Gao, Z. Li, S. Li, Z. Zhou, S. Wei, H. Zhang, An important discovery of high-quality source rocks of marine-continental transitional facies, obtained by Borehole WFD-1, Fuyang area, Anhui Province. *China Geol.* **48**, 1659–1660 (2021).
79. J. Chen, I. P. Montañez, Y. Qi, X. Wang, Q. Wang, W. Lin, Coupled sedimentary and δ¹³C records of late Mississippian platform-to-slope successions from South China: Insight into δ¹³C chemostratigraphy. *Palaeogeogr. Palaeoclimatol. Palaeoecol.* **448**, 162–178 (2016).

Acknowledgments: We also thank X.Q. Zhou, J.F. Xiao, and W. Gao for sampling in the field. We also thank A. Brasier and two anonymous reviewers for constructive reviews. **Funding:** This work was supported by the Chinese Academy of Science (QYZDJ-SSW-DQC005), the National Natural Science Foundation of China (grant nos. 42102123, 91755210, and 42072035), and Youth Innovation Promotion Association CAS (2023418). M.L. is grateful for the SRA grant from the Chinese Academy of Sciences. **Author contributions:** W.Y., M.L., D.C., T.R.T., X.W., and X.F. conceived the study file. W.Y., M.L., D.C., J.C., T.R.T., S.L., C.G., G.Z., and L.Z. performed sampling. W.Y., X.W., and H.Z. performed Hg concentration and isotope measurements and other laboratory work. W.Y. and M.L. analyzed the data. M.L. and W.Y. wrote the draft paper, which was improved by contribution from D.C., Y.-W.X., R.A.S., J.C., T.R.T., X.W., and X.F. and commented on by all authors. D.C. and X.F. offered the funding acquisition. **Competing interests:** The authors declare that they have no competing interests. **Data and materials availability:** All data needed to evaluate the conclusions in the paper are present in the paper and/or the Supplementary Materials.

Submitted 19 September 2022

Accepted 27 March 2023

Published 28 April 2023

10.1126/sciadv.ade9510